

Cite this: *Chem. Sci.*, 2018, 9, 2147

Impact of ambient gases on the mechanism of [Cs₈Nb₆O₁₉]-promoted nerve-agent decomposition†‡

Alexey L. Kaledin,^a Darren M. Driscoll,^b Diego Troya,^b Daniel L. Collins-Wildman,^c Craig L. Hill,^b John R. Morris^{*b} and Djamaladdin G. Musaev^{†ab}

The impact of ambient gas molecules (X), NO₂, CO₂ and SO₂ on the structure, stability and decontamination activity of Cs₈Nb₆O₁₉ polyoxometalate was studied computationally and experimentally. It was found that Cs₈Nb₆O₁₉ absorbs these molecules more strongly than it adsorbs water and Sarin (GB) and that these interactions hinder nerve agent decontamination. The impacts of diamagnetic CO₂ and SO₂ molecules on polyoxoniobate Cs₈Nb₆O₁₉ were fundamentally different from that of NO₂ radical. At ambient temperatures, weak coordination of the first NO₂ radical to Cs₈Nb₆O₁₉ conferred partial radical character on the polyoxoniobate and promoted stronger coordination of the second NO₂ adsorbent to form a stable diamagnetic Cs₈Nb₆O₁₉/(NO₂)₂ species. Moreover, at low temperatures, NO₂ radicals formed stable dinitrogen tetroxide (N₂O₄) that weakly interacted with Cs₈Nb₆O₁₉. It was found that both in the absence and presence of ambient gas molecules, GB decontamination by the Cs₈Nb₆O₁₉ species proceeds *via* general base hydrolysis involving: (a) the adsorption of water and the nerve agent on Cs₈Nb₆O₁₉/(X), (b) concerted hydrolysis of a water molecule on a basic oxygen atom of the polyoxoniobate and nucleophilic addition of the nascent OH group to the phosphorus center of Sarin, and (c) rapid reorganization of the formed pentacoordinated-phosphorus intermediate, followed by dissociation of either HF or isopropanol and formation of POM-bound isopropyl methyl phosphonic acid (i-MPA) or methyl phosphonofluoridic acid (MPFA), respectively. The presence of the ambient gas molecules increases the energy of the intermediate stationary points relative to the asymptote of the reactants and slightly increases the hydrolysis barrier. These changes closely correlate with the Cs₈Nb₆O₁₉-X complexation energy. The most energetically stable intermediates of the GB hydrolysis and decontamination reaction were found to be Cs₈Nb₆O₁₉/X-MPFA-(i-POH) and Cs₈Nb₆O₁₉/X-(i-MPA)-HF both in the absence and presence of ambient gas molecules. The high stability of these intermediates is due to, in part, the strong hydrogen bonding between the adsorbates and the protonated [Cs₈Nb₆O₁₉/X/H]⁺-core. Desorption of HF or/and (i-POH) and regeneration of the catalyst required deprotonation of the [Cs₈Nb₆O₁₉/X/H]⁺-core and protonation of the phosphonic acids i-MPA and MPFA. This catalyst regeneration is shown to be a highly endothermic process, which is the rate-limiting step of the GB hydrolysis and decontamination reaction both in the absence and presence of ambient gas molecules.

Received 21st November 2017
Accepted 5th January 2018

DOI: 10.1039/c7sc04997h

rsc.li/chemical-science

Introduction

The design of materials that can rapidly, fully, and catalytically decontaminate chemical warfare agents (CWAs) and other toxic compounds is an increasingly active area of research and one that presents some questions in fundamental chemistry.^{1–5} As suggested by enzymatic chemistry, some of the most effective strategies for CWA destruction involve catalyzed hydrolysis reactions.⁴ Specifically, it is well established that the P–X bonds (X = F, CN, SR, *etc.*) of organophosphorus (OP) nerve agents rapidly inactivate acetylcholinesterase (a serine hydrolase), the enzyme that facilitates hydrolysis of the neurotransmitter acetylcholine in the nervous system. This inactivation occurs through rapid nucleophilic addition and irreversible binding of

^aC. L. Emerson Center for Scientific Computation and Department of Chemistry, Emory University, Atlanta, Georgia, 30322, USA. E-mail: dmusaev@emory.edu

^bDepartment of Chemistry, Virginia Tech, Blacksburg, Virginia, 24061, USA. E-mail: jmorris@vt.edu

^cDepartment of Chemistry, Emory University, Atlanta, Georgia, 30322, USA. E-mail: chill@emory.edu

† Dedicated to the memory of Prof. Keiji Morokuma.

‡ Electronic supplementary information (ESI) available: (1) The calculated transition states, intermediates and products of the GB hydrolysis and their important geometry parameters (in Å) for X = SO₂, (2) the calculated adsorption energies (in kcal mol⁻¹) of NO₂ radicals to Cs₈Nb₆O₁₉, (3) Cartesian coordinates for all reported structures in xyz format. (structure.xyz). See DOI: 10.1039/c7sc04997h



the serine OH to the phosphorus atom of the nerve agent. Thus, an atomistic/molecular level understanding of the hydrolysis of OP compounds by nucleophilic addition and other processes may lead to the development of more effective materials and catalysts for nerve agent decontamination. Ongoing research efforts have identified several organic and inorganic materials, including metal–organic frameworks (MOFs, especially UiO-66, NU-1000 and MOF-808),^{5–10} polyoxometalates (POMs),^{11–14} MOF/POM hybrid materials,^{15,16} zirconium hydroxide,¹⁷ zeolites,¹⁸ and organic polymers,¹⁹ as effective OP hydrolysis materials.

Recently, the use of POMs to catalyze nerve agent decontamination has attracted wide attention, in part because POMs are molecular representations of metal oxides and are thus far more amenable than the latter to extensive synthetic compositional alteration and characterization at the molecular level.^{20,21} Polyoxoniobates (PONbs), including $[\text{Nb}_6\text{O}_{19}]^{8-}$, are effective OP nerve agent hydrolysis compounds because their high negative charge densities (negative charge per polyanion oxygen) render them highly basic and nucleophilic. Thus, it is not surprising that the synthesis and in-depth analysis of the structures and reactivities of various (alkali and organic) salts of PONbs continue to be the focus of extensive studies.^{22,23} These studies show that the structures and, consequently, the catalytic activities of these materials for nerve agent decontamination depend on many factors, including (but not limited to) the nature of the counter-cation, the pH of the solution, the aggregate state (powder or solid-state material) of the catalyst, the real-time environmental conditions, and the nature and concentration of ambient gas molecules.

Earlier research on Lindqvist hexaniobate alkali salts ($\text{M}_8\text{Nb}_6\text{O}_{19}$, $\text{M} = \text{Li}, \text{K}, \text{Cs}$) reported rapid hydrolysis of the OP agent Sarin (GB, propan-2-yl methylphosphonofluoridate, see Scheme 1) both in aqueous solution and at the gas–surface interface.¹¹ Small-angle X-ray scattering (SAXS) measurements showed aggregation of the OP compounds on the polyoxoniobate (PONb), which led to the suggestion that the reaction follows a general base hydrolysis mechanism.¹² Our subsequent computational study on the mechanism of decomposition of GB by a Cs-salt of PONb, $\text{Cs}_8\text{Nb}_6\text{O}_{19}$ (or CsPONb), confirmed the general base hydrolysis mechanism of this reaction at the gas–surface interface.²⁴

Briefly, we have found that GB degradation by $\text{Cs}_8\text{Nb}_6\text{O}_{19}$ includes the following elementary steps (see Scheme 1): (a) the adsorption of water and the nerve agent on the $\text{Cs}_8\text{Nb}_6\text{O}_{19}$ species, (b) concerted dissociation of the adsorbed water molecule on a basic oxygen atom of the polyoxoniobate and nucleophilic addition of the nascent OH group to the phosphorus center of the nerve agent, (c) rapid reorganization of the resulting pentacoordinated phosphorus intermediate by dissociation of either HF or isopropanol, and formation of POM-bound isopropyl methyl phosphonic acid (i-MPA) or methyl phosphonofluoridic acid (MPFA), respectively. The calculations showed that the phosphonic acids i-MPA and MPFA are strongly bound to the protonated $[\text{Cs}_8\text{Nb}_6\text{O}_{19}\text{H}]^+$ -core through hydrogen bonds and electrostatic interactions with the Cs counter-ions, suggesting that full catalyst regeneration may require additional treatment and depends on the nature of the counter-cations as well as the real-time (ambient) experimental conditions.

Although PONb catalysts have been shown to react with CWAs, the chemistry has yet to be characterized in the presence of ambient gases (for example, NO_2 , CO_2 and SO_2), which may affect the stabilities, structural motifs, and activities of the PONb catalysts. Because this issue is vital to the application of PONbs as decontamination catalysts in real conditions, this paper probes the impact of the common battlefield contaminants NO_2 , CO_2 and SO_2 on the structure, stability and decontamination activity of the exemplary PONb species $\text{Cs}_8\text{Nb}_6\text{O}_{19}$. This study addresses in depth the effects of these ambient gases on the structures of the catalysts and the base hydrolysis mechanism for Sarin degradation using density functional theory (DFT) calculations and infrared (IR) spectroscopy.

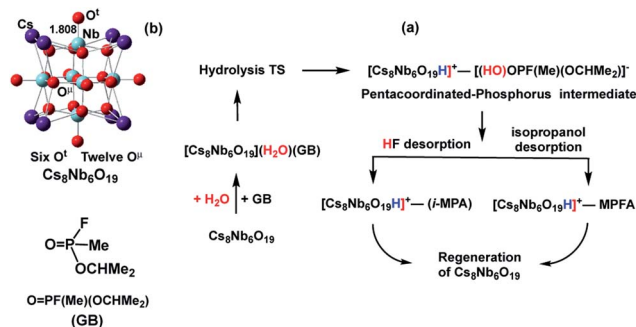
Results and discussion

A. Structure of $\text{Cs}_8\text{Nb}_6\text{O}_{19}$ in the presence of gaseous CO_2 , NO_2 and SO_2

Here, we divide our discussion into two subsections. First, we discuss the interaction of diamagnetic CO_2 and SO_2 molecules with $\text{Cs}_8\text{Nb}_6\text{O}_{19}$; then, we present our findings on the interactions between NO_2 radical and $\text{Cs}_8\text{Nb}_6\text{O}_{19}$.

A1. Structure of $\text{Cs}_8\text{Nb}_6\text{O}_{19}$ in the presence of gaseous CO_2 and SO_2 . Our calculations reveal that $\text{Cs}_8\text{Nb}_6\text{O}_{19}$ very strongly binds the ambient gas molecules CO_2 and SO_2 at various (terminal O^t and/or bridging O^b) sites to form $\text{Cs}_8\text{Nb}_6\text{O}_{19}/\text{X}$ adducts. As reported in Table 1, where we present the calculated adsorption energies, there is a clear preference of adsorption of both CO_2 and SO_2 at the terminal oxygen site rather than at the bridging oxygen site. Indeed, the calculated enthalpies and free energies of adsorption (presented as $\Delta H/\Delta G$) of $\text{Cs}_8\text{Nb}_6\text{O}_{19} + \text{X} \rightarrow \text{Cs}_8\text{Nb}_6\text{O}_{19}/\text{X}$ upon coordination of X to the O^t and O^b sites are $-29.0/-23.2$ and $-16.7/-10.8$ kcal mol⁻¹ for $\text{X} = \text{CO}_2$ and $-47.6/-40.3$ and $-34.1/-26.6$ kcal mol⁻¹ for $\text{X} = \text{SO}_2$, respectively.

The factors that impact the strength of the $\text{Cs}_8\text{Nb}_6\text{O}_{19}/\text{X}$ bonding and site-preference of absorption were analyzed by investigating the resulting geometries of these complexes. From Fig. 1, where we present the most important geometries of the



Scheme 1 Schematics of: (a) the mechanism of Sarin (GB) hydrolysis (reported in ref. 24) promoted by the $\text{Cs}_8\text{Nb}_6\text{O}_{19}$ polyoxoniobate and (b) the $\text{Cs}_8\text{Nb}_6\text{O}_{19}$ polyoxoniobate.



Table 1 Adsorption energies (total electronic E , enthalpy H and Gibbs free energy G in kcal mol⁻¹) defined as energy differences of the complex Cs₈Nb₆O₁₉/ X and its two separated fragments, Cs₈Nb₆O₁₉ + X , where X = CO₂, NO₂ and SO₂, as shown in the leftmost column. The superscripts "t" and "μ" indicate the position where the molecule is adsorbed on Cs₈Nb₆O₁₉; Cs^N indicates NO₂ adsorption to two Cs counter-cations in a symmetric manner

	ΔE	ΔH	ΔG
O ^t : Cs ₈ Nb ₆ O ₁₉ + CO ₂	-29.1	-29.0	-23.2
O ^μ : Cs ₈ Nb ₆ O ₁₉ + CO ₂	-16.8	-16.7	-10.8
O ^t : Cs ₈ Nb ₆ O ₁₉ + SO ₂	-48.2	-47.6	-40.3
O ^μ : Cs ₈ Nb ₆ O ₁₉ + SO ₂	-34.7	-34.1	-26.6
Cs ^N : Cs ₈ Nb ₆ O ₁₉ + NO ₂	-21.7	-22.2	-22.1
O ^t : Cs ₈ Nb ₆ O ₁₉ + NO ₂	-18.8	-18.7	-13.9
Cs ^N and O ^t : Cs ₈ Nb ₆ O ₁₉ + 2NO ₂	-77.4	-74.6	-58.0
Cs ₈ Nb ₆ O ₁₉ /CO ₂ (O ^t) + H ₂ O	-24.2	-22.4	-11.9
Cs ₈ Nb ₆ O ₁₉ /SO ₂ (O ^t) + H ₂ O	-22.7	-21.0	-9.7
Cs ₈ Nb ₆ O ₁₉ + H ₂ O	-24.6	-23.6	-17.3
Cs ₈ Nb ₆ O ₁₉ /H ₂ O + GB	-18.8	-17.4	-4.2
Cs ₈ Nb ₆ O ₁₉ /H ₂ O/CO ₂ (O ^t) + GB	-18.0	-17.4	-2.4
Cs ₈ Nb ₆ O ₁₉ /H ₂ O/SO ₂ (O ^t) + GB	-17.4	-16.4	-3.7

Cs₈Nb₆O₁₉/ X (O^t) and Cs₈Nb₆O₁₉/ X (O^μ) isomeric species for X = CO₂ and SO₂ (for full geometries of these species, see the ESI†), we make the following conclusions:

(a) The CO₂ molecule in Cs₈Nb₆O₁₉/CO₂(O^t) is bound to Cs₈Nb₆O₁₉ *via* multiple interactions, including two (C=O)_{CO₂}...Cs interactions and one C-O^t interaction. The long calculated bond distances for the Cs-O¹, Cs-O² and Cs-C interactions (3.23, 3.25 and 3.28 Å, respectively) indicate they are relatively weak. In contrast, the C-O^t interaction is stronger, with a bond distance of 1.39 Å. As a result of this strong interaction, the Nb-O^t distance is elongated from 1.80 Å to 2.02 Å (see Fig. 1). Thus, while the interactions with the Cs cations provide additional stability to the complex Cs₈Nb₆O₁₉/CO₂(O^t), the primary

interaction occurs between the C atom of CO₂ and the terminal oxygen atom of Cs₈Nb₆O₁₉.

In the Cs₈Nb₆O₁₉/CO₂(O^μ) isomer, where CO₂ interacts with a bridging oxygen, the C-O^μ bond distance is longer (calculated to be 1.44 Å) than the C-O^t bond distance in Cs₈Nb₆O₁₉/CO₂(O^t), while the Cs-O¹ and Cs-O² interactions are slightly stronger (based on the calculated Cs-O¹ and Cs-O² distances). The above presented geometry parameters of Cs₈Nb₆O₁₉/CO₂(O^t) and Cs₈PONb/CO₂(O^μ) not only explain the calculated energy difference between these species, but are also consistent with the amounts of charge transfer from Cs₈Nb₆O₁₉ to CO₂: in the Cs₈Nb₆O₁₉/CO₂(O^t) and Cs₈Nb₆O₁₉/CO₂(O^μ) complexes, almost 0.8 | e | and 0.4 | e | negative charge is transferred from Cs₈Nb₆O₁₉ to CO₂, respectively. Furthermore, the putative CO₃-group in Cs₈Nb₆O₁₉/CO₂(O^t) has a total negative charge of 1.52 | e |.

The strong coordination of CO₂ to Cs₈Nb₆O₁₉ is also supported by IR spectroscopic studies, where the adsorption of CO₂ onto Cs₈Nb₆O₁₉ was investigated by recording the infrared spectra before, during, and after exposure of Cs₈Nb₆O₁₉ to a constant flux of CO₂. Upon adsorption of CO₂ on Cs₈Nb₆O₁₉, three prominent features appeared in the infrared spectrum (Fig. 2, i) at 1659 cm⁻¹, 1290 cm⁻¹ and 1229 cm⁻¹. Interestingly, we observed no feature in the infrared spectrum around 2300 cm⁻¹, which would be associated with a linear CO₂ molecule bound to the POM surface. The 1229 cm⁻¹ and 1290 cm⁻¹ bands are consistent with the IR-inactive symmetric stretch from the gas-phase (ν_1 (C-O)), which becomes IR active upon binding to the POM. The 1659 cm⁻¹ band is likely related to the antisymmetric ν_3 (C-O) stretch of CO₂/CO₃ (occurs at 2349 cm⁻¹ in the gas-phase²⁵ and significantly redshifts upon adsorption). The presence of both the ν_1 and ν_3 bands in the infrared spectrum indicates a bent structure of the adsorbate at the surface. Upon evacuation of CO₂ from the chamber, the 1229 cm⁻¹ spectroscopic feature diminishes, indicating that this band corresponds to the vibrational motion of weakly bound CO₂ species on the surface (Fig. 2, ii); however, the two other features (1659 and 1290 cm⁻¹) persist until annealing the Cs₈Nb₆O₁₉ sample at 423 K (Fig. 2, iii). The elevated

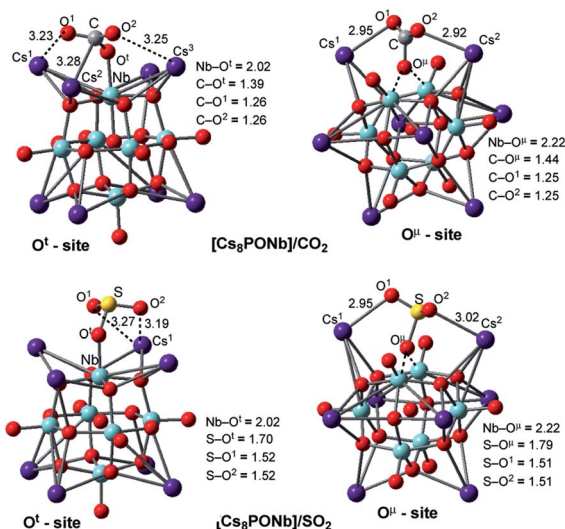


Fig. 1 Adsorption of the ambient gas molecules CO₂ and SO₂ on Cs₈Nb₆O₁₉ at the O^t sites (left) and bridging sites (right) with their important geometry parameters (in Å).

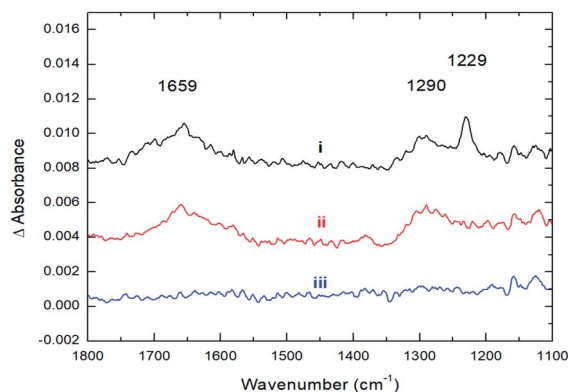


Fig. 2 Infrared spectra recorded during and after the adsorption of CO₂ onto Cs₈Nb₆O₁₉ at 300 K. (i) Adsorption of 100 mTorr of CO₂. (ii) After CO₂ evacuation. (iii) After CO₂ evacuation and thermal treatment at 423 K.



temperature required to fully remove the CO₂ suggests that the molecules responsible for these infrared bands are strongly bound to Cs₈Nb₆O₁₉. The experimentally observed IR features are in full agreement with the DFT calculations (harmonic, unscaled). Indeed, the two prominent IR active features at 1290 and 1659 cm⁻¹, which are ascribed to the bending and asymmetric CO stretch motions of a bent CO₂ molecule, are calculated to be 1316 and 1317 cm⁻¹ (for the bend) and 1702 and 1719 cm⁻¹ (for the asymmetric stretch) in Cs₈Nb₆O₁₉/CO₂(O^l) and Cs₈Nb₆O₁₉/CO₂(O^h), respectively. Thus, the above presented experimental and computational analysis shows that a large fraction of the adsorbed CO₂ strongly binds to Cs₈Nb₆O₁₉. Once at the surface, the molecule adopts a bent geometry, which activates the ν₁ vibrational motion toward absorption of infrared radiation.

(b) The geometric features of Cs₈Nb₆O₁₉/SO₂(O^l) and Cs₈Nb₆O₁₉/SO₂(O^h) adducts are similar to those of their CO₂ analogs: among the interactions, the strongest are the S–O^l and S–O^h interactions, with 1.70 and 1.79 Å bond distances, respectively. These geometry parameters are consistent with the greater stability of the Cs₈Nb₆O₁₉/SO₂(O^l) isomer. Furthermore, comparison of the calculated Cs₈Nb₆O₁₉–X binding energies shows that SO₂ interacts with Cs₈Nb₆O₁₉ much more strongly, by nearly a factor of two, than CO₂. However, both molecules clearly persist on the POM at ambient and well above ambient temperatures.

Further calculations showed that single Cs₈Nb₆O₁₉ species can bind several CO₂ and SO₂ molecules. As seen in Table 2, where we have summarized the adsorption energies as a function of the number of molecules adsorbed at the six O^l sites, there is a pronounced monotonic convergence of the electronic and enthalpy binding energies up to n = 6. The free energies, on the other hand, reveal thermodynamic instability for CO₂ adsorption at larger values of n, suggesting that only the Cs₈Nb₆O₁₉/(CO₂)_n species with n ≤ 4 are viable. The Cs₈Nb₆O₁₉/(SO₂)_n species may still be stable for n > 6.

A2. Structure of Cs₈Nb₆O₁₉ in the presence of NO₂ radicals.

As one might expect, the interaction of Cs₈Nb₆O₁₉ with NO₂ radicals is conceptually different than those discussed above for the diamagnetic CO₂ and SO₂ molecules. Indeed, at first, in the

Table 2 Adsorption of n(X) (X = CO₂ and SO₂ and n = 1 to 6) on Cs₈Nb₆O₁₉ at its O^l-sites, reported as incremental ΔZ_{n,n-1}(Cs₈Nb₆O₁₉/X) = Z_n(Cs₈Nb₆O₁₉/X) – Z_{n-1}(Cs₈Nb₆O₁₉/X) – Z(X) energies (where Z = E, H or G) (in kcal mol⁻¹)

n	X = CO ₂			X = SO ₂		
	Z = E	Z = H	Z = G	Z = E	Z = H	Z = G
1	-29.1	-29.0	-23.2	-48.2	-47.6	-40.3
2	-22.9	-21.8	-11.2	-43.3	-42.4	-27.6
3	-19.6	-18.9	-9.6	-38.8	-37.1	-27.3
4	-13.3	-12.5	-0.7	-34.2	-32.9	-19.8
5	-7.3	-6.6	4.4	-26.9	-25.9	-14.9
6	-2.2	-2.0	6.9	-29.0	-27.9	-16.9

gas-phase and at low temperatures, NO₂ radicals are in equilibrium with dinitrogen tetroxide, N₂O₄, while higher temperatures shift the equilibrium towards nitrogen dioxide.²⁶

The calculations show that N₂O₄ is planar, with an N–N bond distance of 1.85 Å, which is significantly longer than the average N–N single bond length of 1.45 Å; this species has a dimerization energy of ΔE/ΔH/ΔG = 19.8/17.3/5.6 kcal mol⁻¹. Unlike NO₂, N₂O₄ is diamagnetic and coordinates to the Cs₈Nb₆O₁₉ catalyst (see Fig. 3) with a Cs₈Nb₆O₁₉–N₂O₄ interaction energy of ΔE/ΔH/ΔG = -25.3/-25.3/-18.5 kcal mol⁻¹. Secondly, as shown in Table 1 and Fig. 3, the “free” NO₂ radical (at ambient temperature) can interact with polyoxoniobate to form the [Cs₈Nb₆O₁₉]/NO₂ adduct. This adduct exists in two energetically stable isomeric forms, Cs₈Nb₆O₁₉/NO₂(O^l) and Cs₈Nb₆O₁₉/NO₂(Cs^N); the most favorable form is Cs₈Nb₆O₁₉/NO₂(Cs^N), where the N atom of NO₂ interacts with two Cs centers (with Cs¹–N and Cs²–N distances of 3.42 and 3.44 Å). To our surprise, these Cs–N interactions lead to electron transfer from Cs₈Nb₆O₁₉ to NO₂ in Cs₈Nb₆O₁₉/NO₂(Cs^N), as evidenced by population analysis: the calculated Mulliken spin/charge is NO₂(Cs^N) = 0.34/-0.65 |e|. Thus, as a result of these interactions, almost 0.65 |e| charge is transferred from Cs₈Nb₆O₁₉ to NO₂; and, consequently, the Cs₈Nb₆O₁₉ unit develops partial radical character. Further analysis shows that most of the unpaired spin of Cs₈Nb₆O₁₉ is located on the internal O^{IN}-center (~0.24 |e|) and the bridging O^h (~0.14 |e|) located close to the Cs atoms coordinated to NO₂, while the remaining spin is delocalized on all other atoms of the polyoxoniobate. Similarly, but to a lesser extent, NO₂(O^l) has a 0.67/-0.41 |e| spin/charge distribution in the Cs₈Nb₆O₁₉/NO₂(O^l) isomer. The calculated Cs₈Nb₆O₁₉–NO₂ binding energies are ΔH/ΔG = -22.2/-22.1 and -18.7/-13.9 kcal mol⁻¹ in Cs₈Nb₆O₁₉/NO₂(Cs^N) and Cs₈Nb₆O₁₉/NO₂(O^l), respectively.

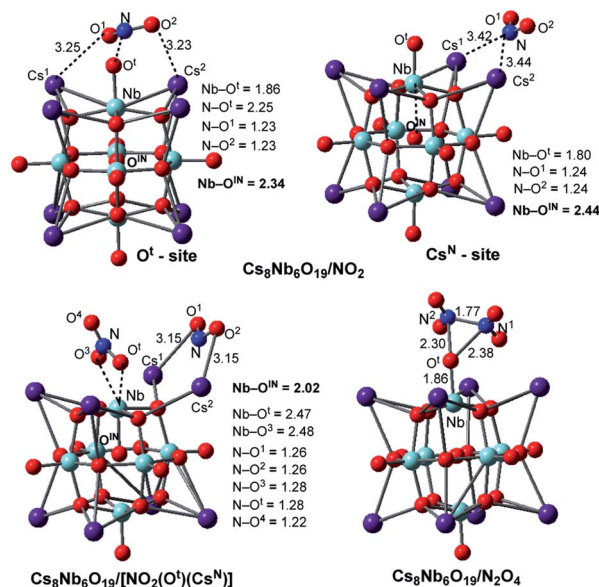


Fig. 3 The calculated most energetically stable structures of NO₂ and N₂O₄ adsorbed on Cs₈Nb₆O₁₉, with their important geometry parameters (in Å).



Consequently, the acquired partial radical character of $\text{Cs}_8\text{Nb}_6\text{O}_{19}$ in the $\text{Cs}_8\text{Nb}_6\text{O}_{19}/\text{NO}_2(\text{Cs}^{\text{N}})$ complex significantly increases its NO_2 -affinity, enabling strong coordination of another (second) NO_2 radical to the O^{t} -site of polyoxoniobate and formation of the most thermodynamically favorable $\text{Cs}_8\text{Nb}_6\text{O}_{19}/[\text{NO}_2(\text{Cs}^{\text{N}})\text{NO}_2(\text{O}^{\text{t}})]$ singlet species. The calculated energy of the reaction $\text{Cs}_8\text{Nb}_6\text{O}_{19}/\text{NO}_2(\text{Cs}^{\text{N}}) + \text{NO}_2 \rightarrow \text{Cs}_8\text{Nb}_6\text{O}_{19}/[\text{NO}_2(\text{Cs}^{\text{N}})\text{NO}_2(\text{O}^{\text{t}})]$ is $\Delta E/\Delta H/\Delta G = -55.8/-52.4/-35.9 \text{ kcal mol}^{-1}$, while the energy of the $\text{Cs}_8\text{Nb}_6\text{O}_{19}/\text{NO}_2(\text{O}^{\text{t}}) + \text{NO}_2 \rightarrow \text{Cs}_8\text{Nb}_6\text{O}_{19}/[\text{NO}_2(\text{Cs}^{\text{N}})\text{NO}_2(\text{O}^{\text{t}})]$ reaction is $\Delta E/\Delta H/\Delta G = -63.8/-61.5/-52.8 \text{ kcal mol}^{-1}$ (see ESI† for more details). Thus, removal of $\text{NO}_2(\text{O}^{\text{t}})$ and/or $\text{NO}_2(\text{Cs}^{\text{N}})$ from $\text{Cs}_8\text{Nb}_6\text{O}_{19}/[\text{NO}_2(\text{Cs}^{\text{N}})\text{NO}_2(\text{O}^{\text{t}})]$ with two NO_2 -adsorbates requires greater energy than removing them from $\text{Cs}_8\text{Nb}_6\text{O}_{19}/\text{NO}_2(\text{O}^{\text{t}})$ and/or $\text{Cs}_8\text{Nb}_6\text{O}_{19}/\text{NO}_2(\text{Cs}^{\text{N}})$. The overall energy of the reaction $\text{Cs}_8\text{Nb}_6\text{O}_{19} + 2\text{NO}_2 \rightarrow \text{Cs}_8\text{Nb}_6\text{O}_{19}/[\text{NO}_2(\text{Cs}^{\text{N}})\text{NO}_2(\text{O}^{\text{t}})]$ is $\Delta E/\Delta H/\Delta G = -77.4/-74.6/-58.0 \text{ kcal mol}^{-1}$ (see Table 1). To summarize, a relatively weak coordination of the first NO_2 radical to $\text{Cs}_8\text{Nb}_6\text{O}_{19}$ at the Cs sites promotes stronger coordination of the second NO_2 molecule at the O^{t} site of $\text{Cs}_8\text{Nb}_6\text{O}_{19}$. As a result, the coordination of the NO_2 radicals to $\text{Cs}_8\text{Nb}_6\text{O}_{19}$ is substantially stronger than that of CO_2 , yet slightly weaker than that of one SO_2 molecule.

The reported highly stable $\text{Cs}_8\text{Nb}_6\text{O}_{19}/[\text{NO}_2(\text{Cs}^{\text{N}})\text{NO}_2(\text{O}^{\text{t}})]$ complex with two NO_2 fragments can also be formed *via* N-N bond activation of the coordinated N_2O_4 molecule by the polyoxometalate catalyst. The former pathway (*i.e.* stepwise addition of two NO_2 radicals to polyoxoniobate) may be valid at ambient temperature, while the latter process may occur at low temperature. In this paper, we did not study the N-N activation barrier; however, we found that the complex $\text{Cs}_8\text{Nb}_6\text{O}_{19}/[\text{NO}_2(\text{Cs}^{\text{N}})\text{NO}_2(\text{O}^{\text{t}})]$ (see Fig. 3) lies significantly lower in energy than the $\text{Cs}_8\text{Nb}_6\text{O}_{19} + \text{N}_2\text{O}_4$ dissociation limit, by $\Delta E/\Delta H/\Delta G = 57.6/57.3/52.4 \text{ kcal mol}^{-1}$, and $\Delta E/\Delta H/\Delta G = 37.8/40.0/46.8 \text{ kcal mol}^{-1}$ lower than the $\text{Cs}_8\text{Nb}_6\text{O}_{19}/\text{N}_2\text{O}_4$ intermediate.

In order to better understand the factors impacting the strength of the $\text{Cs}_8\text{Nb}_6\text{O}_{19}/\text{NO}_2$ interaction, we also analyzed the geometry of the complex $\text{Cs}_8\text{Nb}_6\text{O}_{19}/[\text{NO}_2(\text{Cs}^{\text{N}})\text{NO}_2(\text{O}^{\text{t}})]$. As seen in Fig. 3, where we present the most important geometries of the $\text{Cs}_8\text{Nb}_6\text{O}_{19}/\text{NO}_2(\text{O}^{\text{t}})$, $\text{Cs}_8\text{Nb}_6\text{O}_{19}/\text{NO}_2(\text{Cs}^{\text{N}})$ and $\text{Cs}_8\text{Nb}_6\text{O}_{19}/[\text{NO}_2(\text{Cs}^{\text{N}})\text{NO}_2(\text{O}^{\text{t}})]$ species (for full geometries of these species, see the ESI†), in $\text{Cs}_8\text{Nb}_6\text{O}_{19}/[\text{NO}_2(\text{Cs}^{\text{N}})\text{NO}_2(\text{O}^{\text{t}})]$, the Nb– O^{t} bond is elongated to 2.47 Å; concurrently, the Nb– O^{IN} bonds (which are 2.34, 2.44 and 2.02 Å in these complexes, respectively) and N– O^{t} bonds (which are 1.28 and 2.25 Å in $\text{Cs}_8\text{Nb}_6\text{O}_{19}/[\text{NO}_2(\text{Cs}^{\text{N}})\text{NO}_2(\text{O}^{\text{t}})]$ and $\text{Cs}_8\text{Nb}_6\text{O}_{19}/\text{NO}_2(\text{O}^{\text{t}})$, respectively) are formed. As a result, the complex $\text{Cs}_8\text{Nb}_6\text{O}_{19}/[\text{NO}_2(\text{Cs}^{\text{N}})\text{NO}_2(\text{O}^{\text{t}})]$ has one $\text{NO}_3^{-\delta}$ fragment ($\delta = 0.4$) and one $\text{NO}_2^{-\delta}$ fragment ($\delta = 0.94$) coordinated to the Cs-cations.

Above, we have shown that: (1) at ambient temperatures, a relatively weak coordination of the first NO_2 radical to $\text{Cs}_8\text{Nb}_6\text{O}_{19}$ confers partial radical character on the polyoxoniobate and promotes a stronger coordination of the second NO_2 radical to form a stable diamagnetic $\text{Cs}_8\text{Nb}_6\text{O}_{19}/[\text{NO}_2(\text{Cs}^{\text{N}})\text{NO}_2(\text{O}^{\text{t}})]$ complex, and (2) at low temperatures, coordination of a weakly stable N_2O_4 molecule to $\text{Cs}_8\text{Nb}_6\text{O}_{19}$ followed by facile N-N bond activation leads to the same $\text{Cs}_8\text{Nb}_6\text{O}_{19}/[\text{NO}_2(\text{Cs}^{\text{N}})\text{NO}_2(\text{O}^{\text{t}})]$ complex. Regardless of the formation mechanisms, in

$\text{Cs}_8\text{Nb}_6\text{O}_{19}/[\text{NO}_2(\text{Cs}^{\text{N}})\text{NO}_2(\text{O}^{\text{t}})]$, the coordination of the NO_2 radical positioned at O^{t} to $\text{Cs}_8\text{Nb}_6\text{O}_{19}$ is substantially stronger than that of CO_2 , yet is slightly weaker than that of one SO_2 molecule.

These conclusions from our computations are fully supported by experiments. As with CO_2 , the adsorption of NO_2 onto $\text{Cs}_8\text{Nb}_6\text{O}_{19}$ was probed with the use of infrared spectroscopy. Fig. 4 shows spectra for the interaction between NO_2 and $\text{Cs}_8\text{Nb}_6\text{O}_{19}$. The adsorption of NO_2 on the surface resulted in two infrared vibrational features – one at 1668 cm^{-1} and another at 1240 cm^{-1} (Fig. 4, i). These features are attributed to adsorbate N–O stretches as opposed to POM motions, which appear below 1000 cm^{-1} . Analysis of the calculated $[\text{Cs}_8\text{Nb}_6\text{O}_{19}]\text{--NO}_2$ complexes suggests that the 1668 cm^{-1} feature is likely due to an asymmetric NO stretch originating from the $\text{Cs}_8\text{Nb}_6\text{O}_{19}/\text{N}_2\text{O}_4$ complex, which the calculations (unscaled) show to be at 1813 cm^{-1} . For the other NO_2 complexes, the highest frequency NO stretch is found below 1600 cm^{-1} , *i.e.* at a lower frequency relative to the experimental peak. Taking into account the usual anharmonic correction, these modes will be found to be even further redshifted to lower frequencies. However, if we consider that the calculated asymmetric (strongly IR active) NO stretch of a free NO_2 radical is 1752 cm^{-1} , and the known experimental value²⁵ is 1618 cm^{-1} , the resulting frequency scale factor of 0.92 brings the asymmetric NO stretch of the $\text{Cs}_8\text{Nb}_6\text{O}_{19}/\text{N}_2\text{O}_4$ complex to exactly 1668 cm^{-1} . Moreover, if the measured 1668 and 1240 cm^{-1} peaks originate from the same thermal mixture of diamagnetic complexes, we expect that the 1240 cm^{-1} peak, which persists at higher temperatures (Fig. 4, iii), is due to the $\text{Cs}_8\text{Nb}_6\text{O}_{19}/[\text{NO}_2(\text{Cs}^{\text{N}})\text{NO}_2(\text{O}^{\text{t}})]$ complex, which is much more stable to thermal perturbation than $\text{Cs}_8\text{Nb}_6\text{O}_{19}/\text{N}_2\text{O}_4$. The latter immediately transforms to $\text{Cs}_8\text{Nb}_6\text{O}_{19}/[\text{NO}_2(\text{Cs}^{\text{N}})\text{NO}_2(\text{O}^{\text{t}})]$ upon N-N activation by heating. Indeed, there is a group of IR-active NO stretching motions in the $\text{Cs}_8\text{Nb}_6\text{O}_{19}/[\text{NO}_2(\text{Cs}^{\text{N}})\text{NO}_2(\text{O}^{\text{t}})]$ complex in the 1346 to 1361 cm^{-1} (1238 to 1252 cm^{-1} scaled) region, which captures the measured 1240 cm^{-1} peak.

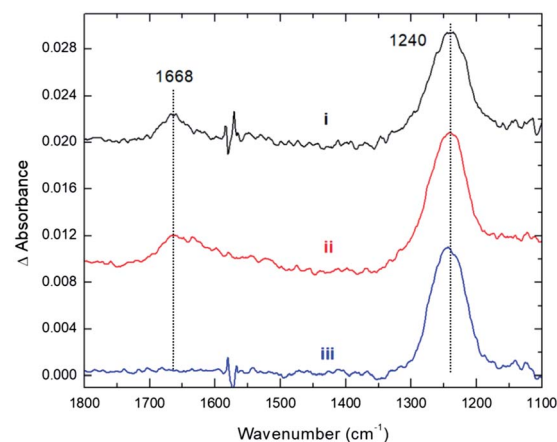


Fig. 4 Infrared spectra recorded during and after the adsorption of NO_2 onto $\text{Cs}_8\text{Nb}_6\text{O}_{19}$ at 300 K. (i) Adsorption of 35 mTorr of NO_2 . (ii) After NO_2 evacuation. (iii) After NO_2 evacuation and thermal treatment at 423 K.



Thus, we present two spectra (shown in Fig. 5); one corresponds to low temperature, Fig. 5(A), which is the sum of $\text{Cs}_8\text{Nb}_6\text{O}_{19}/\text{N}_2\text{O}_4$ and $\text{Cs}_8\text{Nb}_6\text{O}_{19}/[\text{NO}_2(\text{Cs}^{\text{N}})\text{NO}_2(\text{O}^{\text{I}})]$, and one corresponds to high temperature, Fig. 5(B), which is pure $\text{Cs}_8\text{Nb}_6\text{O}_{19}/[\text{NO}_2(\text{Cs}^{\text{N}})\text{NO}_2(\text{O}^{\text{I}})]$. The frequency axis is scaled by the same factor of 0.92. The calculation is consistent with experiments with regard to the disappearance of the 1668 cm^{-1} peak and the persistence of the 1240 cm^{-1} peak. However, the peak at 1470 cm^{-1} (after scaling) in the calculated spectra, which is attributed to a local NO stretch of the NO_3 unit in $\text{Cs}_8\text{Nb}_6\text{O}_{19}/[\text{NO}_2(\text{Cs}^{\text{N}})\text{NO}_2(\text{O}^{\text{I}})]$, is absent in the room-temperature experiments. This suggests that the formation of NO_3 requires a significant amount of thermal energy.

Furthermore, experiments clearly show that NO_2 is strongly bound to the POM, *i.e.* the 1240 cm^{-1} peak is present even after gas phase evacuation (Fig. 4, ii) and upon heating the POM to 423 K (Fig. 4, iii). In fact, thermal treatment up to 600 K was required to fully desorb the species, *i.e.* to remove NO_2 radicals. This suggests that NO_2 binds more strongly to the POM than CO_2 , which is consistent with the computational data for the $\text{Cs}_8\text{Nb}_6\text{O}_{19}/[\text{NO}_2(\text{Cs}^{\text{N}})\text{NO}_2(\text{O}^{\text{I}})]$ complex presented above (see Table 1 and the ESI†).

Thus, the data presented above show that in the presence of ambient gas molecules of CO_2 , NO_2 and SO_2 , $\text{Cs}_8\text{Nb}_6\text{O}_{19}$ will absorb these molecules more strongly than the water and GB molecules required for hydrolysis of Sarin (see Table 1). This is expected to impact the hydrolysis of Sarin by $\text{Cs}_8\text{Nb}_6\text{O}_{19}$ in the following two ways: first, because the ambient gas molecules coordinate to catalytically active O^{I} -centers, they block these catalytically active centers, hindering water and Sarin coordination, and may alter the previously reported mechanism of Sarin hydrolysis by $\text{Cs}_8\text{Nb}_6\text{O}_{19}$. Second, the interaction of an ambient gas molecule with $\text{Cs}_8\text{Nb}_6\text{O}_{19}$ may change the electronic properties of the polyoxoniobate: this is expected to only impact the calculated energetics of the Sarin hydrolysis and to not significantly change the nature of the previously reported intermediates and transition state structures.

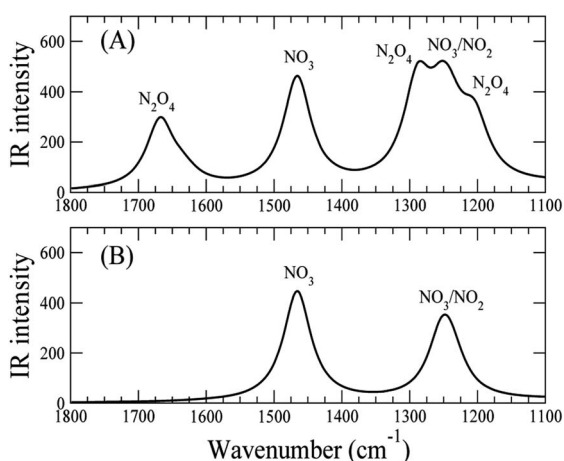


Fig. 5 The calculated harmonic IR spectra (all in the NO stretch region), scaled by 0.92, of (A) the sum of the $\text{Cs}_8\text{Nb}_6\text{O}_{19}/\text{N}_2\text{O}_4$ and $\text{Cs}_8\text{Nb}_6\text{O}_{19}/[\text{NO}_2(\text{Cs}^{\text{N}})\text{NO}_2(\text{O}^{\text{I}})]$ species; (B) the pure $\text{Cs}_8\text{Nb}_6\text{O}_{19}/[\text{NO}_2(\text{Cs}^{\text{N}})\text{NO}_2(\text{O}^{\text{I}})]$ species.

Below, we test the first hypothesis by (a) studying the full potential energy surfaces of GB hydrolysis by $\text{Cs}_8\text{Nb}_6\text{O}_{19}/\text{X}$, where $\text{X} = \text{CO}_2$ and SO_2 , and (b) comparing these new findings with our previous results on the same reaction in the absence of ambient gas molecules. For the sake of simplicity, we discuss in detail only the reaction mechanism (as well as the structures of the pre-reaction complexes, intermediates, transition states and products) for $\text{X} = \text{CO}_2$ and compare these findings with those (previously reported) in the absence of ambient gas molecules. In addition, we briefly discuss, where appropriate, our findings for $\text{X} = \text{SO}_2$ (full potential energy surfaces are available in the ESI†). The reactivities of the NO_2 and other radical species coordinated to $\text{Cs}_8\text{Nb}_6\text{O}_{19}$ will be reported elsewhere.

B. Hydrolysis of Sarin by $\text{Cs}_8\text{Nb}_6\text{O}_{19}/\text{X}$ species (where $\text{X} = \text{CO}_2$ and SO_2)

As we have shown previously²⁴ and have briefly discussed above (see Scheme 1), Sarin hydrolysis by $\text{Cs}_8\text{Nb}_6\text{O}_{19}$ is a multistep process, with coordination of a water molecule to the catalyst as the first step. The calculations (see Table 1) show that coordination of H_2O to $\text{Cs}_8\text{Nb}_6\text{O}_{19}$ to form $\text{Cs}_8\text{Nb}_6\text{O}_{19}/\text{H}_2\text{O}$ is exothermic/exergonic by (presented as $\Delta H/\Delta G$) $23.6/17.3\text{ kcal mol}^{-1}$. In $\text{Cs}_8\text{Nb}_6\text{O}_{19}/\text{H}_2\text{O}$, the two hydrogens of the water molecule interact with one bridging (O^{II}) and one terminal (O^{I}) oxygen atom of the polyoxometalate.

Water molecule coordination to the adduct formed when CO_2 (or SO_2) binds to the O^{I} -center of $\text{Cs}_8\text{Nb}_6\text{O}_{19}$ is a few kcal mol^{-1} less than that for “free” $\text{Cs}_8\text{Nb}_6\text{O}_{19}$; the energies are $-22.4/-11.9$ and $-21.0/-9.7\text{ kcal mol}^{-1}$ for $\text{X} = \text{CO}_2$ and SO_2 , respectively. This effect is more pronounced for the $\text{Cs}_8\text{Nb}_6\text{O}_{19}/\text{SO}_2$ adduct than for $\text{Cs}_8\text{Nb}_6\text{O}_{19}/\text{CO}_2$. Furthermore, as seen in Fig. 6, the water coordination motif in $\text{Cs}_8\text{Nb}_6\text{O}_{19}/\text{CO}_2/\text{H}_2\text{O}$ is different from that in $\text{Cs}_8\text{Nb}_6\text{O}_{19}/\text{H}_2\text{O}$: because CO_2 occupies the O^{I} -position in $\text{Cs}_8\text{Nb}_6\text{O}_{19}/\text{CO}_2$, the H_2O molecule is H-bonded to one bridging (O^{II}) and one CO (O^{I}) oxygen atom (instead of O^{I}). The calculated $\text{O}^{\text{II}}-\text{H}^1$ and $\text{O}^{\text{I}}-\text{H}^2$ bond distances are 1.76 and 1.85 \AA , respectively.

Following the formation of the $\text{Cs}_8\text{Nb}_6\text{O}_{19}/\text{X}/\text{H}_2\text{O}$ complex, the addition of Sarin to this intermediate occurs. Previously, we examined several approaches of Sarin to $\text{Cs}_8\text{Nb}_6\text{O}_{19}$ and found that nerve agent decomposition occurs when Sarin approaches the hydrated $\text{Cs}_8\text{Nb}_6\text{O}_{19}$ segment with its $\text{O}(\text{sp}^2)$ and $\text{O}(\text{sp}^3)$ atoms (labeled in Fig. 6 and below as O^5 and O^4 , respectively).²⁴ The additional stabilization of the complex arises from the long-range $\text{O}^4\cdots\text{Cs}^3$ ionic interaction. Thus, for the purposes of modeling the decomposition of Sarin in the presence of carbon and sulfur dioxide, it is sufficient to examine the most energetically favorable pathway, similar to that previously reported for the case with no ambient gas molecules. In keeping with the previously established shorthand notation, the pre-reaction complex of this reaction pathway is labeled as R-F_X.

The present calculations show that the coordination of Sarin (GB) to $\text{Cs}_8\text{Nb}_6\text{O}_{19}/\text{X}/\text{H}_2\text{O}$ is exothermic by $-18.0/-2.4$ and $-17.4/-3.8\text{ kcal mol}^{-1}$ for $\text{X} = \text{CO}_2$ and SO_2 , respectively. Inspection of the structure of the $\text{Cs}_8\text{Nb}_6\text{O}_{19}/\text{X}/\text{H}_2\text{O}/\text{GB}$, R-F_X, intermediate reveals a non-covalently bonded $[\text{Cs}_8\text{Nb}_6\text{O}_{19}/\text{CO}_2/\text{H}_2\text{O}]\text{-GB}$ complex. For example, as seen in Fig. 6, in contrast to



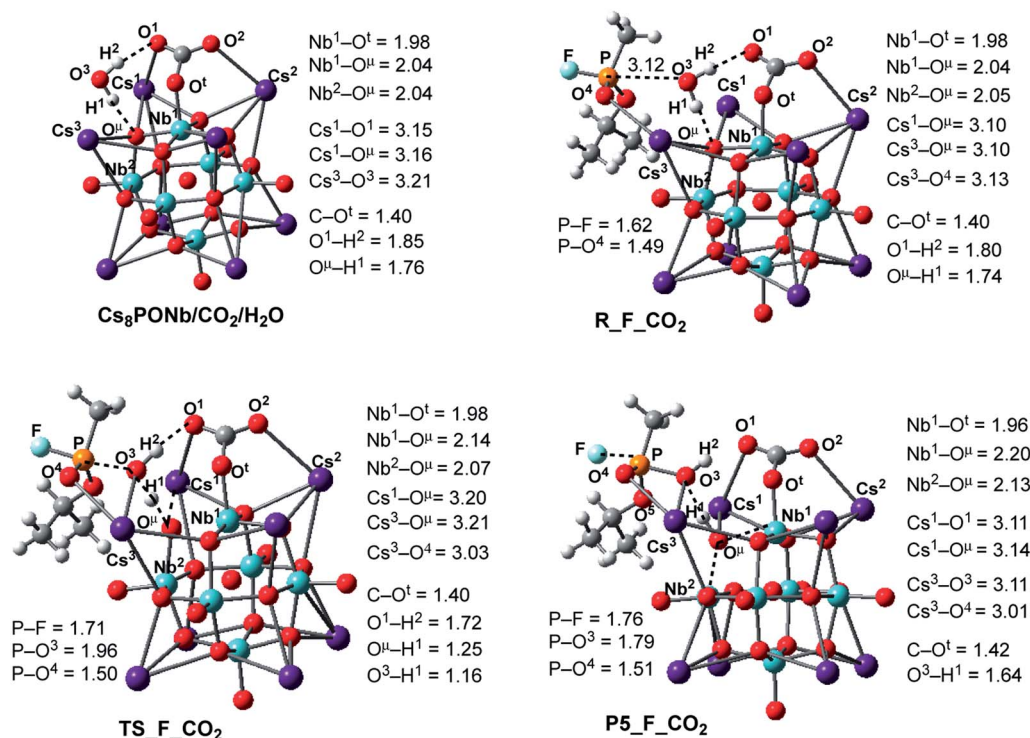


Fig. 6 Calculated pre-reaction complexes, transition states and products of GB hydrolysis by $\text{Cs}_8\text{Nb}_6\text{O}_{19}/\text{CO}_2$ (i.e. the reaction $\text{Cs}_8\text{Nb}_6\text{O}_{19}/\text{CO}_2 + \text{H}_2\text{O} + \text{GB} \rightarrow \text{R-F-}\text{CO}_2 \rightarrow \text{TS-F-}\text{CO}_2 \rightarrow \text{P5-F-}\text{CO}_2$) and their important geometry parameters (in Å). Similar structures for $\text{X} = \text{SO}_2$ are presented in the ESI.†

the coordination of GB to $\text{Cs}_8\text{Nb}_6\text{O}_{19}/\text{H}_2\text{O}$, in $\text{Cs}_8\text{Nb}_6\text{O}_{19}/\text{CO}_2/\text{H}_2\text{O}/\text{GB}$, the nerve agent is coordinated to one of the Cs centers of the $\text{Cs}_8\text{Nb}_6\text{O}_{19}$ -core with its $\text{P}=\text{O}^4$ double bond. Several H-bonds also exist between the GB ligand and the $[\text{Cs}_8\text{Nb}_6\text{O}_{19}/\text{CO}_2/\text{H}_2\text{O}]$ -fragment. In this complex, the calculated Cs^3-O^4 bond distance is 3.13 Å and the nascent $\text{P}-\text{O}^3(\text{OH}_2)$ bond distance is 3.12 Å.

In the next step, hydrolysis of the coordinated water molecule occurs between the coordinated gas molecule X, the bridging oxygen (O^μ) of the $\text{Cs}_8\text{Nb}_6\text{O}_{19}$ -core and the phosphorus center of Sarin. The transition state associated with this process, $\text{TS-F-}\text{CO}_2$, is shown in Fig. 6 (for $\text{TS-F-}\text{SO}_2$, see the ESI.†). As seen in this figure, at $\text{TS-F-}\text{CO}_2$, the breaking O^3-H^1 bond of the water molecule is elongated to 1.16 Å, and the forming $\text{O}^\mu-\text{H}^1$ bond distance becomes 1.25 Å. In addition, Nb^1-O^μ and Nb^2-O^μ bonds are slightly elongated and the Cs^3-O^4 bond is slightly shortened. Importantly, the Cs^3 -center of the $\text{Cs}_8\text{Nb}_6\text{O}_{19}$ core also interacts with the oxygen (O^3) of water and provides additional support for hydrolysis. Here, the other coordinates of interest are the $\text{P}-\text{O}^3(\text{H}_2\text{O})$ bond and the $\text{P}-\text{F}$ bond.

As seen in Fig. 6, $\text{P}-\text{O}^3(\text{H}_2\text{O})$ undergoes a major reduction from 3.12 Å in $\text{R-F-}\text{CO}_2$ to 1.96 Å in $\text{TS-F-}\text{CO}_2$. Its $\text{P}-\text{F}$ counterpart, located *trans* to the water-activated molecule, extends from the typical single bond in $\text{R-F-}\text{CO}_2$, with an increase from 1.62 Å to 1.71 Å in $\text{TS-F-}\text{CO}_2$. Similar geometry changes at the hydrolysis transition state were observed for $\text{X} = \text{SO}_2$ (see the ESI.†). As seen in Fig. 7, the calculated $\Delta E/\Delta G$ barrier heights relative to

R-F-X are 7.8/7.5 and 8.4/8.8 kcal mol^{-1} for $\text{X} = \text{CO}_2$ and SO_2 , respectively. These values are slightly larger than the values of 6.8/6.1 kcal mol^{-1} calculated for the reaction in the absence of these ambient gas molecules; this suggests that common battlefield contaminants may impair the hydrolytic decomposition of nerve agents under operational conditions.

The hydrolysis product is a pentacoordinated-phosphorus complex P5-F-X with a trigonal bipyramidal structure around the central phosphorus atom. In our previous paper, we showed that this intermediate exhibits multiple isomeric forms.²⁴ Here, we discuss only the energetically most favorable form, which is directly connected to the transition state TS-F-X . For example,

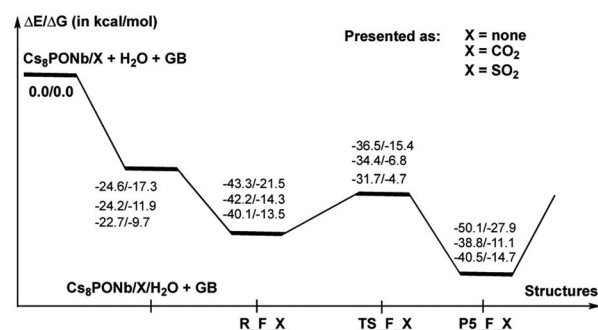


Fig. 7 Potential energy profile of the hydrolysis of Sarin (GB) by $\text{Cs}_8\text{Nb}_6\text{O}_{19}$ and $\text{Cs}_8\text{Nb}_6\text{O}_{19}/\text{X}(\text{O}^t)$, where $\text{X} = \text{CO}_2$ or SO_2 . ΔE and ΔG are the changes in the electronic and Gibbs free energies and are calculated relative to the reactants $\text{Cs}_8\text{Nb}_6\text{O}_{19}/\text{X}(\text{O}^t) + \text{H}_2\text{O} + \text{GB}$.



as seen in Fig. 6, the formed P–O³ bond in P5-F_CO₂ contracts to 1.79 Å, while its P–F counterpart, located *trans* to the activated water molecule, extends to 1.76 Å. The broken O³–H¹ bond is elongated to 1.64 Å and the Nb¹–Oⁱⁱ and Nb²–Oⁱⁱ bonds are elongated to 2.20 and 2.13 Å, respectively. Concurrently, the Cs³–O³ bond of 3.11 Å is formed to provide additional stabilization to the pentacoordinated-phosphorus complex, similar to that previously reported in P5-F.²⁴ Based on the calculated Mulliken charge distribution, the resulting P5-F_X complexes can be labeled as a [(GBOH[−])(Cs₈Nb₆O₁₉H/X)]⁺ ion-pair system.

As shown in Fig. 7, the hydrolysis of Sarin, *i.e.* the reaction Cs₈Nb₆O₁₉/X + H₂O + GB → R-F_X → TS-F_X → P5-F_X for X = none, CO₂ or SO₂, is exergonic by −50.1/−27.9, −38.8/−11.1 and −40.5/−14.7 kcal mol^{−1} (presented as ΔH/ΔG) and proceeds over energy barriers of 6.8/6.1, 7.5/7.5 and 8.4/8.8 kcal mol^{−1} (calculated relative to the pre-reaction intermediate R-F_X), respectively. The reaction R-F_X → TS-F_X → P5-F_X is exothermic for X = none and SO₂ by 6.8/6.4 and 0.4/1.2 kcal mol^{−1}, respectively, but is endothermic by 3.4/3.2 kcal mol^{−1} for X = CO₂. These energy values allow us to conclude that the presence of ambient gas molecules increases the energies of the stationary points relative to the asymptote of the reactants. This is likely the result of a different charge distribution on Cs₈Nb₆O₁₉/X relative to Cs₈Nb₆O₁₉, where X acquires a net negative charge of 0.8 to 0.7 |e|, as we showed above. Furthermore, X coordinates to the Oⁱ reactive center and disables its hydrolytic activity. The presence of ambient gases increases the hydrolysis barrier by 1.0 to 2.5 kcal mol^{−1}, and this change in the energy barrier is closely associated with the Cs₈Nb₆O₁₉–X complexation energy: the stronger the Cs₈Nb₆O₁₉–X bond, the higher the barrier for Sarin hydrolysis.

C. Pentacoordinated P5-F_X intermediate dissociation

Once the pentacoordinated P5-F_X species is formed, the reaction can proceed along several paths, as discussed in our previous paper.²⁴ In order to evaluate the role of the catalyst in the course of the reaction, as above, here we discuss in detail only those pathways that directly involve the catalyst. These are the HF and isopropanol elimination and, ultimately, desorption pathways. The accompanying products of these paths are isopropyl methyl phosphonic acid (i-MPA) and methyl phosphonofluoridic acid (MPFA), respectively. It is evident that in order to form HF or isopropanol, protonation of the fluoride or oxygen centers of the isopropoxy ligand is required. Furthermore, in order to facilitate regeneration of the catalyst, the ultimate proton source should be the OⁱⁱH¹-group of the [Cs₈Nb₆O₁₉H/X]⁺ cation. However, these processes are expected to be very complex and may proceed *via* multiple mechanisms. One of these processes could involve any surrounding water molecules, which are expected to be present in real experimental conditions. In this mechanism, a water molecule located close to the fluoride or oxygen atoms of the isopropoxy ligand is expected to donate its proton to these groups (to form HF and/or isopropanol, respectively) and compensate by removing the proton from the OⁱⁱH¹-group of the catalyst *via*

a H-bonding network. This process depends on multiple factors (including, but not limited to, the concentration of water in the system and the reaction temperature) and was not studied in this paper.

Another possible mechanism of HF and/or isopropanol formation is direct removal of the proton from the OⁱⁱH¹-group of the catalyst by the fluoride and/or isopropoxide ligands, respectively. As shown previously for the Cs₈Nb₆O₁₉ catalyst (*i.e.*, in the absence of ambient gas molecules),²⁴ these processes occur with very small energy barriers which have no contribution to the overall outcome of the decontamination reaction but lead to the most energetically stable intermediates, Cs₈Nb₆O₁₉-(i-MPA)-HF and Cs₈Nb₆O₁₉-(MPFA)-(i-POH), respectively (see Fig. 8). Here, we performed an extensive search to locate the transition states TS2-F_HF_X and TS2-F_(i-POH)_X that lead to either HF and i-MPA or isopropanol (i-POH) and MPFA from the most stable pentacoordinated intermediate P5-F_X (where X = CO₂ or SO₂). Ultimately, we were able to locate only the TS2-F_(i-POH)_X transition state (see Fig. 8). The search for the HF formation transition state TS2-F_HF_X was unsuccessful and always led to either the Cs₈Nb₆O₁₉/X-(i-MPA)-HF intermediate, its derivative F[−]⋯H⁺⋯Oⁱⁱ intermediate, or the pre-reaction complex P5-F_X. For example, in Fig. 8, we present the intermediates, transition states and products involved in pentacoordinated P5-F_CO₂ intermediate dissociation alone, with their important geometry parameters (for those of X = SO₂, see the ESI[†]). The relative energies of these species, calculated from the P5-F_X pre-reaction complex, are given in Fig. 9.

As seen in Fig. 8, at the transition state TS2-F_(i-POH)_CO₂ associated with the formation of i-POH and MPFA, the activated P–O⁵(Osp²) bond extends to 2.19 Å from 1.68 Å in P5-F_CO₂, with simultaneous formation of a double H-bond network (O⁵–H¹ = 1.63 Å and O¹–H² = 1.57 Å) as a precursor to the

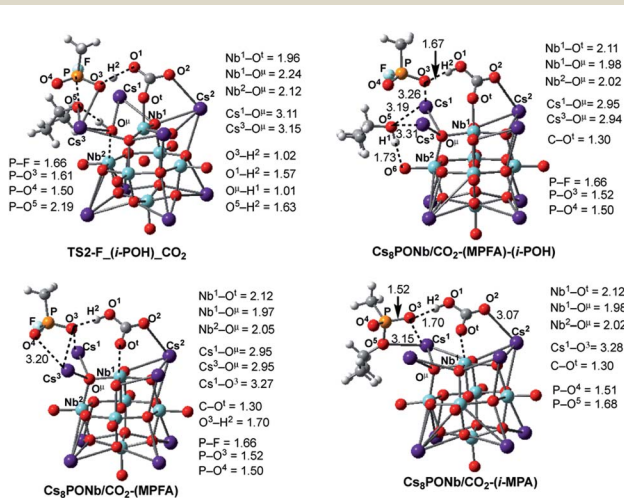


Fig. 8 The calculated transition states, intermediates and products of the dissociation of pentacoordinated P5-F_CO₂ (*i.e.* reactions: P5-F_CO₂ → Cs₈Nb₆O₁₉/CO₂-(MPFA)-(i-POH) → Cs₈Nb₆O₁₉/CO₂ + MPFAH + (i-POH) and P5-F_X → Cs₈Nb₆O₁₉/CO₂-(i-MPA)-HF → Cs₈Nb₆O₁₉/CO₂ + MPAH + HF) with their important geometry parameters (in Å). Similar structures for X = SO₂ are presented in the ESI[†].



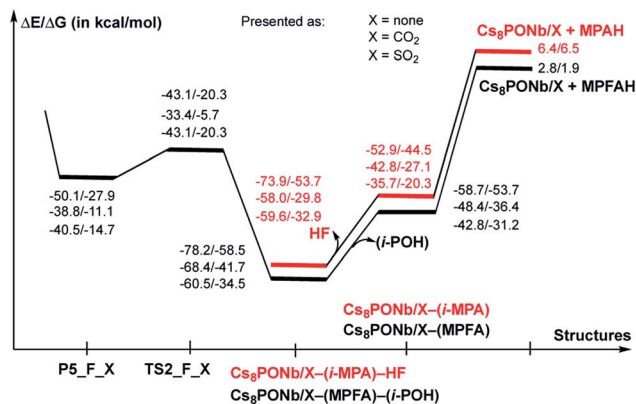


Fig. 9 Potential energy profiles of the decomposition reaction of pentacoordinated-phosphorus intermediate P5-F_X, where X = CO₂ and SO₂ (i.e. reactions: P5-F_X → Cs₈Nb₆O₁₉/X-(MPFA)-(i-POH) → Cs₈Nb₆O₁₉/X + MPFAH + (i-POH) and P5-F_X → Cs₈Nb₆O₁₉/X-(MPA)-HF → Cs₈Nb₆O₁₉/X + MPAH + HF). ΔE and ΔG are the changes in the electronic and Gibbs free energies and are calculated relative to the reactants Cs₈Nb₆O₁₉/X(O^t) + H₂O + GB.

charge-preserving double proton transfer. In other words, as the proton of the O^HH¹-group moves to Sarin, the proton on the PO³H¹ group of Sarin migrates back to the Cs₈Nb₆O₁₉/X-core to form [HXO^t]^q, where X = CO₂. As a result, the formed P-O³(H₂O) bond is shortened from 1.79 Å in P5-F_CO₂ to 1.61 Å in the transition state.

As seen in Fig. 9, the calculated energy barriers from P5-F_X are 7.0/7.6, 5.4/5.4 and 3.6/6.5 kcal mol⁻¹ for X = none, CO₂ and SO₂. Thus, the presence of these gas molecules in the reaction mixture slightly reduces the pentacoordinated P5-F_X intermediate dissociation barrier (by 2 to 4 kcal mol⁻¹). Furthermore, the changes in the i-POH and MPFA formation energy barriers correlate with the Cs₈Nb₆O₁₉-X complexation energy: the stronger the Cs₈Nb₆O₁₉-X bond, the smaller the i-POH and MPFA formation energy barriers.

Comparison of the calculated energetics for the dissociation of the pentacoordinated intermediate with those for hydrolysis (i.e. formation of the pentacoordinated intermediate) show that, in general, the hydrolysis step is a rate-determining step for all reported species, and the presence of ambient gas molecules increases this energy barrier only slightly, by 2 to 4 kcal mol⁻¹. Furthermore, the height of this rate-determining energy barrier correlates with the Cs₈Nb₆O₁₉-X complexation energy: the stronger the Cs₈Nb₆O₁₉-X bond, the more difficult the hydrolysis of GB by the Cs₈Nb₆O₁₉ catalyst.

D. Catalyst regeneration

Thus, the facile dissociation of the P5_F_X species, as reported previously for P5_F, yields HF and i-MPA and/or i-POH and MPFA products. All these species are initially bound to Cs₈Nb₆O₁₉, as shown in Fig. 8 for X = CO₂ and the ES1[‡] for X = SO₂. For example, in the Cs₈Nb₆O₁₉/CO₂-(i-MPA)-HF complex, the (i-MPA)-fragment forms a hydrogen bond with the O^H and OH-unit of the HOCOO^t fragment, respectively. The HF molecule, on the other hand, in the presence of an X molecule,

prefers to form an [F⁻⋯H⁺] ion-pair prior to dissociation. Similarly, in the Cs₈Nb₆O₁₉/CO₂-(MPFA)-(i-POH) complex, the (i-POH) molecule and MPFA-fragment are hydrogen bonded to another O^t atom and the OH-unit of the HOCOO^t fragment, respectively; the calculated H¹-O⁶ and O³-H² bond distances are 1.73 and 1.67 Å, respectively. In addition, there are electrostatic interactions between the O center of the isopropanol molecule and two Cs cations of the Cs₈Nb₆O₁₉/CO₂ core, with Cs¹-O⁵ and Cs³-O⁵ bond distances of 3.19 Å and 3.31 Å, respectively. The formed P-O³ fragment also interacts with the Cs¹-center, with a Cs¹-O³ distance of 3.16 Å.

As seen in Fig. 9, the formed Cs₈Nb₆O₁₉/X-MPFA-(i-POH) is the energetically lowest structure on the potential energy surface of the entire GB hydrolysis and decontamination reaction by Cs₈Nb₆O₁₉ both in the absence and presence of ambient gas molecules. The intermediate Cs₈Nb₆O₁₉/X-(i-MPA)-HF is found to be only slightly higher in energy. As we mentioned previously,²⁴ the high stability of these intermediates is due in part to the strong hydrogen bonds between the adsorbates and the Cs₈Nb₆O₁₉/X-core; however, it is also due to the additional stabilizing interactions between the Cs counter-ions and the electronegative atoms of the nerve-agent fragments.

Desorption of HF and isopropanol from Cs₈Nb₆O₁₉/X-(i-MPA)-HF and Cs₈Nb₆O₁₉/X-MPFA-(i-POH) requires 15.2/12.7 and 20.0/5.3 kcal mol⁻¹ energy, respectively, for X = CO₂. Dissociation of HF and isopropanol only slightly modifies the geometries of the products Cs₈Nb₆O₁₉/X-(i-MPA) and Cs₈Nb₆O₁₉/X-MPFA fragments (for example, see Fig. 8 for X = CO₂) compared with the Cs₈Nb₆O₁₉/X-(i-MPA)-HF and Cs₈Nb₆O₁₉/X-MPFA-(i-POH) adducts; therefore, this will not be discussed in detail.

However, both i-MPA in Cs₈Nb₆O₁₉/X-(i-MPA) and MPFA in Cs₈Nb₆O₁₉/X-MPFA are strongly bound to the protonated [Cs₈Nb₆O₁₉/X]H⁺-core. Thus, regeneration of the catalyst requires deprotonation of the [Cs₈Nb₆O₁₉/X]H⁺-core and protonation of the phosphonic acids i-MPA and MPFA. This step of the reaction, which forms a final decontaminated form of the GB and re-generated catalyst, is found to be highly endothermic/endergonic, i.e. 6.4/6.5 and 2.8/1.9 kcal mol⁻¹ for i-MPAH and MPFAH formation, respectively. Overall, the last steps of the reaction, i.e. the reactions Cs₈Nb₆O₁₉/X-(i-MPA)-HF → Cs₈Nb₆O₁₉/X + HF + (i-MPAH) and Cs₈Nb₆O₁₉/X-MPFA-(i-POH) → Cs₈Nb₆O₁₉/X + (i-POH) + MPFAH, are highly prohibitive and require energies of 80.3/60.2 (X = none), 64.4/36.3 (X = CO₂), and 66.0/39.4 (X = SO₂) kcal mol⁻¹ and 81.0/60.4 (X = none), 71.2/43.6 (X = CO₂), and 63.3/36.4 (X = SO₂) kcal mol⁻¹, respectively. Furthermore, deprotonation of the [Cs₈Nb₆O₁₉/X]H⁺-core and protonation of the phosphonic acids i-MPA and MPFA is expected to be very complex and may proceed *via* several pathways depending on the reaction conditions. One of these may involve any surrounding water molecules, in real experimental conditions, *via* a concerted protonation-deprotonation mechanism involving the hydrogen-bonded water-based network. However, this process depends on multiple factors (including, but not limited to, the concentration of water in the system and the reaction temperature) and was not studied in this paper. We also failed to locate a transition state associated with the direct deprotonation of



$[\text{Cs}_8\text{Nb}_6\text{O}_{19}/\text{X}]\text{H}^+$ and protonation of the phosphonic acids because of the high stability of the corresponding pre-reaction complexes $\text{Cs}_8\text{Nb}_6\text{O}_{19}/\text{X}(\text{i-MPA})$ and $\text{Cs}_8\text{Nb}_6\text{O}_{19}/\text{X-MPFA}$. The solution to this issue requires special comprehensive experimental and computational studies, which are in progress.

Conclusions

This paper, for the first time, addresses the impact of environmentally-significant ambient gas molecules, NO_2 , CO_2 and SO_2 , on the structure, stability and decontamination activity of a basic polyoxometalate species. Specifically, $\text{Cs}_8\text{Nb}_6\text{O}_{19}$ in the presence of these gases has been studied in depth by complementary computational and experimental approaches. It was found that:

(1) $\text{Cs}_8\text{Nb}_6\text{O}_{19}$ absorbs ambient gas molecules of $\text{X} = \text{CO}_2$, NO_2 and SO_2 more strongly than it absorbs water or Sarin (GB) molecules. The calculated $\text{Cs}_8\text{Nb}_6\text{O}_{19}\text{-X}$ binding energy follows the trend for $\Delta G (\text{X} = \text{CO}_2) < \Delta G (\text{NO}_2) < \Delta G (\text{SO}_2)$.

(2) The impacts of the diamagnetic CO_2 and SO_2 molecules on polyoxoniobate $\text{Cs}_8\text{Nb}_6\text{O}_{19}$ are fundamentally different than that of the NO_2 radical. At ambient temperatures, weak coordination of the first NO_2 radical to $\text{Cs}_8\text{Nb}_6\text{O}_{19}$ confers partial radical character on the polyoxoniobate and promotes a stronger coordination of the second NO_2 radical to form a stable diamagnetic $\text{Cs}_8\text{Nb}_6\text{O}_{19}/(\text{NO}_2)_2$ species; meanwhile, at low temperatures, NO_2 radicals form weakly stable dinitrogen tetraoxide (N_2O_4), which interacts weakly with $\text{Cs}_8\text{Nb}_6\text{O}_{19}$.

(3) Similar to the case without ambient gas molecules, reported previously,²⁴ in the presence of X, GB hydrolysis by $\text{Cs}_8\text{Nb}_6\text{O}_{19}/\text{X}$ proceeds *via* general base hydrolysis involving: (a) adsorption of water and the nerve agent on the $\text{Cs}_8\text{Nb}_6\text{O}_{19}/\text{X}$ catalyst, (b) concerted hydrolysis of the adsorbed water molecule on a basic oxygen atom of the polyoxoniobate and nucleophilic addition of the nascent OH group to the phosphorus center of the nerve agent, (c) rapid reorganization of the resulting pentacoordinated-phosphorus intermediate followed by dissociation of either HF or isopropanol with formation of POM-bound isopropyl methyl phosphonic acid (i-MPA) or methyl phosphonofluoridic acid (MPFA), respectively.

(4) $\text{Cs}_8\text{Nb}_6\text{O}_{19}$ adsorbs ambient gas molecules X at its basic O^t (or O^h) reactive centers, which shields them from involvement in the base hydrolysis. As a result, one of the O centers of the coordinated ambient gas molecule becomes an active hydrolysis center. This increases the energies of the stationary points relative to the asymptote of the reactants and increases the hydrolysis barrier. These changes are closely correlated with the $\text{Cs}_8\text{Nb}_6\text{O}_{19}\text{-X}$ complexation energy; the stronger the $\text{Cs}_8\text{Nb}_6\text{O}_{19}\text{-X}$ bond, the higher the barrier for Sarin hydrolysis.

(5) The most energetically stable products of the GB hydrolysis and decontamination reaction are $\text{Cs}_8\text{Nb}_6\text{O}_{19}/\text{X-MPFA}(\text{i-POH})$ and $\text{Cs}_8\text{Nb}_6\text{O}_{19}/\text{X}(\text{i-MPA})\text{-HF}$ both in the absence and presence of ambient gas molecules. The high stability of these intermediates is due in part to the strong hydrogen bonds between the adsorbates and the protonated $[\text{Cs}_8\text{Nb}_6\text{O}_{19}/\text{X}/\text{H}]^+$ -core and to interactions between the Cs counterions and the electronegative atoms of the adsorbates.

(6) Desorption of HF or/and (i-POH) and regeneration of the catalyst requires deprotonation of the $[\text{Cs}_8\text{Nb}_6\text{O}_{19}/\text{X}/\text{H}]^+$ -core with protonation of the phosphonic acids i-MPA and MPFA. Regeneration of the catalyst is a highly endergonic process and is the rate-limiting step for GB hydrolytic decontamination, both in the absence and presence of ambient gas molecules.

Notes

A. Computational and experimental procedures

A1. Computational methodology. A major computational challenge in the present work is to properly describe the non-covalent interactions involving the various ions in the systems studied: the Cs^+ counter-cations, $[\text{Nb}_6\text{O}_{19}]^{8-}$ with its large negative charge, and the H^+ and OH^- ions resulting from heterolytic water dissociation. These interactions are expected to be well described by the M06-L density functional,²⁷ a pure density functional designed for transition metal bonding and non-covalent interactions. Therefore, all presented calculations have been carried out with the M06-L density functional, as implemented in the Gaussian09 code.²⁸ In these calculations, we used the 6-31++G(d,p) basis set for the elements S, P, F, O, C, H and the LanL2dz basis set with corresponding Hay-Wadt effective core potentials for Nb and Cs, as implemented in Gaussian09. The sets of diffuse functions (++) were added specifically to obtain proper descriptions of the diffuse charge densities and long-range interactions. All reported stationary points were confirmed to have either all real frequencies (minima) or one imaginary frequency (transition states). The latter were further verified to connect the corresponding minima by IRC calculations. All reported enthalpy and Gibbs free energies were computed at a temperature of 298.15 K and 1 atm pressure.

A2. Experimental methodology. The synthesis of $\text{Cs}_8\text{Nb}_6\text{O}_{19}\cdot 14\text{H}_2\text{O}$ followed a known literature procedure. A solution of cesium hydroxide (14.6 g, 50% by weight) was heated to 90 °C in an Erlenmeyer flask. 5 g of hydrous, amorphous niobium oxide was added in small portions, with full dissolution of each portion before addition of the subsequent portion. Evaporative crystallization yielded giant hexagonal crystals.

Infrared spectroscopic experiments were performed in a stainless-steel high-vacuum chamber with a base pressure of $\sim 1 \times 10^{-8}$ Torr. The $\text{Cs}_8\text{Nb}_6\text{O}_{19}$ sample was pressed, as a 7 mm diameter disk, into a tungsten grid, which was then clamped onto a sample mount coupled to a precision manipulator. An empty region of the grid was used to monitor the gas phase species in the chamber and was also employed as a background for surface adsorption and desorption studies. The grid was resistively heated, and the temperature was monitored *via* a K-type thermocouple spot-welded adjacent to the sample. A PID controller mediated the sample temperature to within ± 1 K. Details of the vacuum chamber and sample mount can be found in a previous publication.²⁹ An FTIR spectrometer (Thermo, Nicolet, Nexus 470 FTIR) with an external liquid- N_2 -cooled MCT-A detector and a spectral resolution of 2 cm^{-1} was used for collection of the infrared spectra.



Conflicts of interest

There are no conflicts to declare.

Acknowledgements

This material is based upon work supported by the U. S. Army Research Laboratory and the U. S. Army Research Office under grant number W911NF-15-2-0107. The authors are grateful for the support of the Defence Threat Reduction Agency. The authors gratefully acknowledge NSF MRI-R2 grant (CHE-0958205 for D. G. M.) and the use of the resources of the Cherry Emerson Center for Scientific Computation.

Notes and references

- (a) F. M. Raushel, *Nature*, 2011, **469**, 310; (b) M. Enserink, *Science*, 2013, **341**, 1050; (c) M. B. D. Nikitin, P. K. Kerr and A. Feickert, *Syria's Chemical Weapons: Issues for Congress*, 2013, report # R42848.
- (a) N. Sharma and R. Kakkar, *Adv. Mater. Lett.*, 2013, **4**, 508; (b) N. Munro, *Environ. Health Perspect.*, 1994, **102**, 18; (c) W. W. George, in *Nanoscale Materials in Chemistry: Environmental Applications*, American Chemical Society, 2010, vol. 1045, pp. 125–136.
- R. H. Pastel and E. C. Ritchie, in *Psychological Responses to the New Terrorism: A NATO-Russia Dialogue*, IOS Press, Amsterdam, 2005, pp. 9–24.
- (a) Y. J. Yang, K. Kim, O. G. Tsay, D. A. Atwood and D. G. Churchill, *Chem. Rev.*, 2015, **115**, PR1; (b) Y. C. Yang, J. A. Baker and J. R. Ward, *Chem. Rev.*, 1992, **92**, 1729.
- J. B. DeCoste and G. W. Peterson, *Chem. Rev.*, 2014, **114**, 5695.
- S. Y. Moon, G. W. Wagner, J. E. Mondloch, G. W. Peterson, J. B. DeCoste, J. T. Hupp and O. K. Farha, *Inorg. Chem.*, 2015, **54**, 10829.
- Y. Liu, S. Y. Moon, J. T. Hupp and O. K. Farha, *ACS Nano*, 2015, **9**, 12358.
- J. E. Mondloch, M. J. Katz, W. C. Isley, P. Ghosh, P. L. Liao, W. Bury, G. W. Wagner, M. G. Hall, J. B. DeCoste, G. W. Peterson, R. Q. Snurr, C. J. Cramer, J. T. Hupp and O. K. Farha, *Nat. Mater.*, 2015, **14**, 512.
- M. J. Katz, J. E. Mondloch, R. K. Totten, J. K. Park, S. T. Nguyen, O. K. Farha and J. T. Hupp, *Angew. Chem., Int. Ed.*, 2014, **53**, 497.
- R. Gaillac, P. Pullumbi, K. A. Beyer, K. W. Chapman, D. A. Keen, T. D. Bennett and F.-X. Coudert, *Nat. Mater.*, 2017, **16**, 1149–1154.
- M. K. Kinnan, W. R. Creasy, L. B. Fullmer, H. L. Schreuder-Gibson and M. Nyman, *Eur. J. Inorg. Chem.*, 2014, **2014**, 2361.
- W. Guo, H. Lv, K. P. Sullivan, W. O. Gordon, A. Balboa, G. W. Wagner, D. G. Musaev, J. Bacsá and C. L. Hill, *Angew. Chem., Int. Ed.*, 2016, **55**, 7403.
- (a) D. M. Mizrahi, S. Saphier and I. Columbus, *J. Hazard. Mater.*, 2010, **179**, 495; (b) N. M. Okun, J. C. Tarr, D. A. Hilleshiem, L. Zhang, K. I. Hardcastle and C. L. Hill, *J. Mol. Catal. A: Chem.*, 2006, **246**, 11; (c) N. M. Okun, T. M. Anderson and C. L. Hill, *J. Mol. Catal. A: Chem.*, 2003, **197**, 283; (d) F. Carniato, C. Bisio, R. Psaro, L. Marchese and M. Guidotti, *Angew. Chem., Int. Ed.*, 2014, **53**, 10095.
- As an example for computational studies of the POMs see: (a) J. M. Poblet, X. Lopez and C. Bo, *Chem. Soc. Rev.*, 2003, **32**, 297; (b) P. Miro, J. M. Poblet, J. B. Avalos and C. Bo, *Can. J. Biochem.*, 2009, **87**, 1296; (c) C. Bo and J. M. Poblet, *Isr. J. Chem.*, 2011, **51**, 228; (d) X. Lopez, P. Miro, J. J. Carbo, A. Rodriguez-Fortea, C. Bo and J. M. Poblet, *Theor. Chem. Acc.*, 2011, **128**, 393; (e) X. Lopez, J. J. Carbo, C. Bo and J. M. Poblet, *Chem. Soc. Rev.*, 2012, **41**, 7537; (f) B. Matt, X. Xiang, A. L. Kaledin, N. N. Han, J. Moussa, H. Amouri, S. Alves, C. L. Hill, T. Q. Lian, D. G. Musaev, G. Izzet and A. Proust, *Chem. Sci.*, 2013, **4**, 1737; (g) A. E. Kuznetsov, Y. V. Geletii, C. L. Hill, K. Morokuma and D. C. Musaev, *J. Am. Chem. Soc.*, 2009, **131**, 6844.
- J. Song, Z. Luo, D. K. Britt, H. Furukawa, O. M. Yaghi, K. I. Hardcastle and C. L. Hill, *J. Am. Chem. Soc.*, 2011, **133**, 16839.
- F. J. Ma, S. X. Liu, C. Y. Sun, D. D. Liang, G. J. Ren, F. Wei, Y. G. Chen and Z. M. Su, *J. Am. Chem. Soc.*, 2011, **133**, 4178.
- T. J. Bandosz, M. Laskoski, J. Mahle, G. Mogilevsky, G. W. Peterson, J. A. Rossin and G. W. Wagner, *J. Phys. Chem. C*, 2012, **116**, 11606.
- S. W. Yang, D. C. Doetschman, J. T. Schulte, J. B. Sarnbur, C. W. Kanyi and J. D. Fox, *Microporous Mesoporous Mater.*, 2006, **92**, 56.
- L. Bromberg, H. Schreuder-Gibson, W. R. Creasy, D. J. McGarvey, R. A. Fry and T. A. Hatton, *Ind. Eng. Chem. Res.*, 2009, **48**, 1650.
- (a) M. K. Kinnan, W. R. Creasy, L. B. Fullmer, H. L. Schreuder-Gibson and M. Nyman, *Eur. J. Inorg. Chem.*, 2014, **2014**, 2361; (b) F.-J. Ma, S.-X. Liu, C.-Y. Sun, D.-D. Liang, G.-J. Ren, F. Wei, Y.-G. Chen and Z.-M. Su, *J. Am. Chem. Soc.*, 2011, **133**, 4178; (c) D. M. Mizrahi, S. Saphier and I. Columbus, *J. Hazard. Mater.*, 2010, **179**, 495–499; (d) N. M. Okun, J. C. Tarr, D. A. Hilleshiem, L. Zhang, K. I. Hardcastle and C. L. Hill, *J. Mol. Catal. A: Chem.*, 2006, **246**, 11; (e) N. M. Okun, T. M. Anderson and C. L. Hill, *J. Mol. Catal. A: Chem.*, 2003, **197**, 283; (f) F. Carniato, C. Bisio, R. Psaro, L. Marchese and M. Guidotti, *Angew. Chem., Int. Ed.*, 2014, **53**, 10095.
- (a) T. Yamase and M. T. Pope, in *Nanostructure Science and Technology*, ed. D. J. Lockwood, Kluwer Academic/Plenum Publishers, New York, vol. 2, 2002; (b) M. T. Pope, in *Comprehensive Coordination Chemistry II: From Biology to Nanotechnology*, ed. A. G. Wedd, Elsevier Ltd., Oxford, UK, 2004, vol. 4, pp. 635–678; (c) H. N. Miras, J. Yan, D.-L. Long and L. Cronin, *Chem. Soc. Rev.*, 2012, **41**, 7403; (d) H. Lv, Y. V. Geletii, C. Zhao, J. W. Vickers, G. Zhu, Z. Luo, J. Song, T. Lian, D. G. Musaev and C. L. Hill, *Chem. Soc. Rev.*, 2012, **41**, 7572.
- (a) M. R. Antonio, M. Nyman and T. M. Anderson, *Angew. Chem., Int. Ed.*, 2009, **121**, 6252; (b) M. Nyman, T. M. Alam, F. Bonhomme, M. A. Rodriguez, C. S. Frazer and M. E. Welk, *J. Cluster Sci.*, 2006, **17**, 197; (c) M. Nyman,



- Dalton Trans.*, 2011, **40**, 8049; (d) E. M. Villa, C. A. Ohlin, E. Balogh, T. M. Anderson, M. D. Nyman and W. H. Casey, *Angew. Chem., Int. Ed.*, 2008, **47**, 4844; (e) E. Balogh, T. M. Anderson, J. R. Rustad, M. Nyman and W. H. Casey, *Inorg. Chem.*, 2007, **46**, 7032.
- 23 M. Nyman, F. Bonhomme, T. M. Alam, M. A. Rodriguez, B. R. Cherry, J. L. Krumhansl, T. M. Nenoff and A. M. Sattler, *Science*, 2002, **297**, 996.
- 24 R. C. Chapleski Jr, D. G. Musaev, C. L. Hill and D. Troya, *J. Phys. Chem. C*, 2016, **120**, 16822.
- 25 T. Shimanouchi, *Tables of molecular vibrational frequencies*, National Bureau of Standards, U.S. Govt. Print. Off., Washington, 1972.
- 26 (a) H. A. Bent, *Inorg. Chem.*, 1963, **2**, 747; (b) E. Wiberg, N. Wiberg and A. F. Holleman, *Inorganic Chemistry*, Academic Press, San Diego, 2001, ISBN 0-12-352651-5.
- 27 Y. Zhao and D. G. Truhlar, *J. Chem. Phys.*, 2006, **125**, 194101.
- 28 M. J. Frisch, G. W. Trucks, H. B. Schlegel, G. E. Scuseria, M. A. Robb, J. R. Cheeseman, G. Scalmani, V. Barone, B. Mennucci, G. A. Petersson, H. Nakatsuji, M. Caricato, X. Li, H. P. Hratchian, A. F. Izmaylov, J. Bloino, G. Zheng, J. L. Sonnenberg, M. Hada, M. Ehara, K. Toyota, R. Fukuda, J. Hasegawa, M. Ishida, T. Nakajima, Y. Honda, O. Kitao, H. Nakai, T. Vreven, J. A. Montgomery Jr, J. E. Peralta, F. J. Ogliaro, M. J. Bearpark, J. Heyd, E. N. Brothers, K. N. Kudin, V. N. Staroverov, R. Kobayashi, J. Normand, K. Raghavachari, A. P. Rendell, J. C. Burant, S. S. Iyengar, J. Tomasi, M. Cossi, N. Rega, N. J. Millam, M. Klene, J. E. Knox, J. B. Cross, V. Bakken, C. Adamo, J. Jaramillo, R. Gomperts, R. E. Stratmann, O. Yazyev, A. J. Austin, R. Cammi, C. Pomelli, J. W. Ochterski, R. L. Martin, K. Morokuma, V. G. Zakrzewski, G. A. Voth, P. Salvador, J. J. Dannenberg, A. Dapprich, A. D. Daniels, J. J. Farkas, J. B. Foresman, J. V. Ortiz, J. Cioslowski and D. J. Fox, Gaussian, Inc.: Wallingford, CT, USA, 2009.
- 29 P. Basu, T. H. Ballinger and J. T. Yates, *Rev. Sci. Instrum.*, 1988, **59**, 1321.

